Cluster analysis of quantitative parametric maps from DCE-MRI: application in evaluating heterogeneity of tumor response to antiangiogenic treatment

Dario Livio Longo, PhD [a,b,c], Walter Dastrù PhD [b,c], Lorena Consolino, MS [b,c], Miklos Espak, PhD [d], Maddalena Arigoni, PhD [c], Federica Cavallo, PhD [c], Silvio Aime, PhD [b,c*]

[a] Institute of Biostructure and Bioimaging (CNR) c/o Molecular Biotechnologies Center, Via Nizza 52, 10126, Torino, Italy

[b] Molecular Imaging Center, University of Torino, Via Nizza 52, 10126 Torino, Italy

[c] Department of Molecular Biotechnology and Health Sciences, University of Torino, Via Nizza 52, 10126 Torino, Italy

[d] Dept. of Computer Science, University College London, Gower Street, London WC1E 6BT, United Kingdom

*Corresponding author:

Silvio Aime, Dipartimento di Biotecnologie Molecolari e Scienze per la Salute, Centro di Imaging Molecolare, Università di Torino, Via Nizza 52, 10126, Torino, Italy.

e-mail: silvio.aime@unito.it, Phone: +39-011-6706451, Fax: +39-011-6706487.

Abstract

Purpose: The objective of this study was to compare a clustering approach to conventional analysis methods for assessing changes in pharmacokinetic parameters obtained from dynamic contrast-enhanced magnetic resonance imaging (DCE-MRI) during antiangiogenic treatment in a breast cancer model.

Materials and methods: BALB/c mice bearing established transplantable her2+ tumors were treated with a DNA-based antiangiogenic vaccine or with an empty plasmid (untreated group). DCE-MRI was carried out by administering a dose of 0.05 mmol/kg of Gadocoletic acid trisodium salt, a Gd-based blood pool contrast agent (CA) at 1T. Changes in pharmacokinetic estimates (K^{trans} and v_p) in a nine-day interval were compared between treated and untreated groups on a voxel-by-voxel analysis. The tumor response to therapy was assessed by a clustering approach and compared with conventional summary statistics, with sub-regions analysis and with histogram analysis.

Results: Both the K^{trans} and v_p estimates, following blood-pool CA injection, showed marked and spatial heterogeneous changes with antiangiogenic treatment. Averaged values for the whole tumor region, as well as from the rim/core sub-regions analysis were unable to assess the antiangiogenic response. Histogram analysis resulted in significant changes only in the v_p estimates ($p<0.05$). The proposed clustering approach depicted marked changes in both the K^{trans} and v_p estimates, with significant spatial heterogeneity in v_p maps in response to treatment ($p<0.05$), provided that DCE-MRI data are properly clustered in three or four sub-regions.

Conclusions: This study demonstrated the value of cluster analysis applied to pharmacokinetic DCE-MRI parametric maps for assessing tumor response to antiangiogenic therapy.

1. Introduction

Tumor angiogenesis is a key process for solid tumors to survive, grow and metastatize [1]. The development of novel anticancer strategies targeting the angiogenic step calls for imaging methods able to assess the early response to new antiangiogenic treatments, comprising vascular disrupting agents (which destroy existing vessels) or antiangiogenic drugs (which block new vessels formation) [2, 3].

Dynamic contrast-enhanced magnetic resonance imaging (DCE-MRI) is the methodology of choice for the evaluation of tumor angiogenesis, and it has been proposed as an imaging biomarker of drug efficacy in phase I clinical trials of angiogenesis inhibitors [4]. DCE-MRI allows investigating microvascular structure and function by tracking the pharmacokinetics of an injected Gd-based contrast agent (CA) as it passes through the tumor vasculature. The obtained enhancement patterns reflect vascular perfusion and permeability of the tumor, showing the potential to monitor changes in the tumor microvasculature following antiangiogenic therapy [5-7]. Despite these promising capabilities, clinical adoption of DCE-MRI as an imaging biomarker is still hampered by challenges related to the lack of standardized methods for both image acquisition and quantification.

Two methods are currently employed to analyze DCE-MRI data to yield quantitative (pharmacokinetic modelling) or semiquantitative (shape analysis) results, respectively. In the semiquantitative approach, features directly obtained from the signal intensity time curve (e.g. maximum relative enhancement, initial slope, time to peak, area under the curve) are used to get a simple description of the CA distribution [8]. These parameters depend on a combination of blood flow, permeability, perfusion and blood volume, therefore represent composite information of the underlying physiological processes. A major drawback of this approach is that it is quite susceptible to minor changes in acquisition protocols, sequence parameters and individual examinations, making direct comparison difficult. In the quantitative approach, pharmacokinetic models are applied to contrast agent concentration data to enable estimates of physiological parameters, including plasma volume (v_p), forward vascular transfer constant (K^{trans}) and the reverse vascular transfer constant (k_{ep}). Several pharmacokinetic models have been proposed since the seminal papers by Tofts and Brix [9, 10], either requiring a measured/assumed arterial input function (AIF), or neglecting the need for the AIF as in the reference region models [11].

The values of the biomarkers derived from the analysis of the DCE-MRI data strongly depend on the characteristics of the CAs used. This affects the overall ability to assess tumor microvasculature. Clinical studies have been carried out mainly by using small-sized Gd-containing contrast media (i.e. gadoteridol), whereas at pre-clinical level several contrast agents having different size and

protein binding capability have been investigated, either at intermediate or high magnetic field (2-4.7T) [12-15]. Intermediate molecular weight (MW) and macromolecular CAs have been shown to be more sensitive to changes in vascular permeability upon antiangiogenic therapies in comparison to low molecular weight CAs thanks to their reduced extravasation in healthy tissues [12, 16, 17]. Even though many efforts have been devoted in the last years to optimize the relaxometric properties and the HSA binding affinities of the CA (in order to attain improved contrast enhancement characteristics)[18-21], to date, only one blood pool Gd-based CA has entered into clinical practice. We have recently shown that, exploiting the magnetic field-dependence of the Gd-complexes relaxivity, intermediate MW Gd-based agents show greater performance at 1T [22]. In addition, high temporal resolution is not a stringent requirement for intermediate MW-enhanced MRI [23, 24].

During growth, tumors develop a highly heterogeneous microenvironment, characterized by severe structural abnormalities of the microvasculature network [25]. Furthermore, it has been shown that treatment of tumors with antiangiogenic drugs promote alternative angiogenic growth factor pathways, further contributing to the increased tumor heterogeneity [26]. There is an overall agreement in considering tumor heterogeneity as one of the key factors of the disease. It is directly related to some tumor properties and reflects its ability to respond/escape to therapeutic treatments [4, 27]. Conversely, the values of the DCE-MRI estimates are therefore strongly dependent on how the tumor ROIs are drawn and on the applied statistic analysis. So far, there is no consensus on which is the optimal method for tumor heterogeneity assessment. ROIs can be drawn to encompass the entire tumor region, or to split the tumor into regions which are spatially defined (poorly enhanced inner regions or core and strongly enhanced periphery regions or rim) [28]. Consequently, the spatial heterogeneity information is discarded by current quantitative analysis methods employing simple summary statistics (e.g. mean or median values on the whole tumor region) or by pre-defined rigid boundaries between rim and core regions [29]. Histogram analysis is considered to be more sensitive in detecting changes in tumor heterogeneity after treatment, than conventional summary statistics, looking to changes in histogram shape (kurtosis) and asymmetry (skewness), although it does so at the expense of including spatial information [28, 30]. Alternative techniques are those based on texture-analysis, providing quantitative estimates of tumor heterogeneity, also considering their spatial distribution [31]. Similarly, novel methods based on clustering approaches, aiming at grouping pixels sharing similar enhancement properties, have been recently proposed. However, to date, clustering methods have only been used for classification of time intensity curve shapes [32] and for discriminating between benign and malign lesions [8, 33] or combined with diffusion based multispectral analysis techniques [34].

The purpose of this study is to investigate the ability of a clustering approach on assessing tumor heterogeneity and thereof changes in the evaluation of the response to a DNA-based antiangiogenic treatment employing a blood-pool contrast agent at 1 T. Within the clustering approach, based on a pixel-by-pixel analysis, the whole tumor has been segmented into several sub-regions according to their enhancement/permeability properties. Moreover, we evaluated if the number of clusters may influence the ability to assess the response to the antiangiogenic treatment. In addition, a quantitative comparison with conventional summary statistics (mean values on the whole tumor or mean values on rim/core tumor sub-regions), and with histogram analysis (skewness and kurtosis) was performed, to test the ability of the clustering approach on the assessment of subtle spatial changes following the therapeutic protocol.

2. Material and methods

2.1. Contrast Agent

Gadocoletic acid trisodium salt (B22956/1), a Gd-based blood pool CA with high affinity for human serum albumin (relaxivity of 25 mM^{-1} s^{-1} at 40 MHz in human serum at 298 K [35]) was kindly provided by Bracco Imaging S.p.A. (Colleretto Giacosa, Italy).

2.2. Animal Studies and antiangiogenic DNA vaccination

Animal studies were approved by the local ethics committee of our University and carried out in accordance with the EU guidelines under Directive 2010/63. Wild type BALB/c mice (n=12) were injected subcutaneously in the inguinal region with 1×10^5 TUBO cells (a cloned Her2/neu+ cell line established from a lobular carcinoma of a BALB-neuT mouse [36]). Mice were vaccinated by electroporation with DNA plasmid coding human p80 Amot (pAmot or Angiomotin) and control pcDNA3 (generated as previously described [37]) when tumor mass reached 4 mm mean diameter and, again, 7 days after. Briefly, 50 μg of plasmid in 20 μl of 0.9% NaCl were injected in the quadriceps muscle of anesthetized mice n = 6 for both treated (Angiomotin plasmid) and untreated (pcDNA3 plasmid) groups, respectively. Immediately after the injection, two 25 ms trans-cutaneous electric low voltage pulses (150 V amplitude) separated by a 300ms interval were administered at the injection site via a multiple needle electrode connected to an electroporator (Cliniporator™, IGEA s.r.l., Carpi, Italy).

All animals were maintained under specific pathogen-free conditions inside the animal facility and received standard rodent chow and had free access to tap water.

2.3. MRI Protocols

Magnetic resonance images were acquired on anesthetized mice with an Aspect M2 MRI System (Aspect Magnet Technologies Ltd., Netanya, Israel) working at 1 Tesla. The anesthetized animals were warmed with a heat lamp before MRI and then wrapped in warm towels to maintain body temperature and placed supine in a transmit/receive solenoid coil with an inner diameter of 3.5 cm. A phantom filled with diluted gadoteridol (Bracco Imaging SpA, Milan, Italy) was included in the field of view (FOV), close to each animal, as a reference, to allow correction for changes in the instrument performance. After the scout image acquisition, a T_2-weighted (T_{2w}) anatomical image was acquired with a Fast Spin Echo sequence (TR 2500 s; TE effective 41 ms; number of slices 10; slice thickness 1.5 mm; FOV 40 mm; acquisition matrix 128×128; four averages; acquisition time 2 m 40 s).

Baseline T_1 maps were acquired using the variable flip angle (VFA) method with a 2D spoiled gradient echo sequence with the following flip angle values: 15°-30°-45°-60°-75°-160° and the same geometry of the anatomical image (TR 40 ms; TE 1.8 ms; number of slices 10; slice thickness 1.5 mm; FOV 40 mm; acquisition matrix 128×128). The accuracy has been validated comparing T1 estimates using an Inversion Recovery Spin Echo imaging sequence (Fig. S1).

DCE–MRI was performed using an axial 2D T_{1w} spoiled gradient echo sequence (TR 40 ms; TE 1.8 ms; flip angle 75°; number of slices 10; slice thickness 1.5 mm; FOV 40 mm; acquisition matrix 128×128; 58 s per image volume). The dynamic imaging protocol consisted of three baseline acquisition followed by the manual injection of Gadocoletic acid trisodium salt through the tail vein at a dose of 0.05 mmol/kg (ca. 60-80 µL within 10 s); 47 dynamic post-contrast images were acquired over a period of 45 min. DCE acquisitions were performed 1 day before the first (PRE) and 1 day after the second (POST) vaccination in two groups of mice vaccinated with Angiomotin (n = 6, treated group) or with pcDNA3 (n = 6, untreated group), respectively.

Mice were anesthetized by injecting a mixture of tiletamine/zolazepam (Zoletil 100; Virbac, Milan, Italy) 20 mg/kg and xylazine (Rompun; Bayer, Milan, Italy) 5 mg/kg and placed in a 30 mm insert coil. Breath rate was monitored throughout *in vivo* MRI experiments using a respiratory probe (SAII Instruments, Stony Brook, NY - USA).

2.4 DCE-MRI Analysis

All the DCE-MRI images were analyzed using an in-house developed software in C++ code implementing MITK (http://www.mitk.org/MITK), ITK and VTK libraries for the quantification of pharmaco-kinetic parameters and in Matlab (MathWorks, Natick, MA) for the comparison between clustering, histogram and simple summary analysis.

2.4.1 Quantitative Analysis

DCE images were coregistered by using a rigid body registration algorithm which searches for the optimal rotation and translational parameters by minimizing the mean squared difference between the moving and the reference image as cost function [38].

Pre-contrast T_1 has been determined using a variable flip angle fast gradient echo technique [39]. Dynamic post-contrast T_1 relaxation was calculated from the SI curves after conversion into longitudinal relaxation rate R_1 ($1/T_1$) assuming a linear relationship between R_1 and CA concentration according to the following equation:

$$C_t(t) = \frac{1/T_1 - 1/T_{10}}{r_{1p}}$$

Where $1/T_{10}$ is the pre contrast longitudinal relaxation rate, $1/T_1$ is the post contrast longitudinal relaxation rate and r_{1p} is the longitudinal relaxivity of the contrast agent that was assumed to be equal to the value (25 mM^{-1} s^{-1}) measured in blood serum. The extended Tofts' model with a individually measured arterial input function (AIF) has been used.[9]. This model assumes a bidirectional exchange between two compartments, the intravascular and the extravascular extracellular space (EES). In order to extract the kinetic parameters (K^{trans}, v_p and k_{ep}) on a voxel-by-voxel basis, the concentration curve in the tissue $C_t(t)$ has been fitted against the solution of the differential equation:

$$C_t(t) = v_p C_p(t) + K^{trans}\left[C_p(t) \otimes e^{-k_{ep}(t)}\right]$$

where $C_t(t)$ is the contrast agent concentration in the tissue at time t, v_p is the fractional blood plasma volume, $C_p(t)$ is the contrast agent blood plasma concentration at time t (AIF), K^{trans} is the volume transfer constant between the intravascular and the EES ($K^{trans} = k_{ep}v_e$), k_{ep} is the rate constant from EES to blood plasma and $\otimes$ is the convolution operator. The AIF and the injection time have been automatically determined by the software using a three-dimensional region growing algorithm with an artery seed point automatically determined from the maximum increase of signal enhancement in the dynamic series. The results of the automated AIF detection methods were inspected visually to confirm that the AIF voxels identified were located within the abdominal aorta and this procedure succeeded for all the analyzed mice (Fig. S2). The parametric maps were further

post-processed to discard voxels that showed poor quality of fit by calculating the root mean squared error (RMSE):

$$RMSE = \sqrt{\frac{\int_{i=1}^{n}(M_i - E_i)^2}{\int_{i=1}^{n}(E_i)^2}}$$

where E and M are experimental and modeled data, respectively. A RMSE threshold value of 0.75 was empirically determined according to the overall signal-to-noise ratio in the DCE-MRI data being analyzed. Voxels showing non-physiological estimates for pharmacokinetic parameters (i.e., values outside of the following ranges: $0 < K^{trans} < 1$ min^{-1}, $0 < v_p < 1$ or $0 < v_e < 1$) were also excluded before they were included in the statistics. Muscle region showed v_e values in the physiological range of about 0.07 ± 0.03 (Fig. S3).

For each tumor, a region of interest (ROI) was manually drawn by the same operator encompassing all the tumor volume taking the T_{2w} images as reference.

2.4.2 Simple summary analysis

The three-dimensional ROIs encompassing the whole tumors were directly applied to the parametric maps, and for each animal, the mean and standard deviations of K^{trans} and v_p values were calculated for the whole tumor.

2.4.3 Regional rim/core analysis

For regional analysis of DCE-MRI parameters, tumor quantitative estimates were evaluated by calculating mean values for pixels in the rim region (defined as the outer area having 1/3 of the diameter of tumor) and in the core region (defined as the inner area having 2/3 of the diameter of tumor) [40].

2.4.4 Histogram analysis

Histogram analyses were applied to the quantitative parametric maps defined by tumor ROIs, calculating skewness (representing the distribution pattern around the mean) and kurtosis (indicating the position of the peak height) measures [41].

2.4.5 Cluster analysis

Partitioning all tumor pixels into k sets (or clusters) was done by exploiting a k-means algorithm using a Euclidean distance [42]. Parametric maps were clustered independently, testing different numbers of clusters: two, three and four. Each cluster consists of voxels that exhibit a similar value,

such that the within-cluster sum of squares (Euclidean distance) between the voxel value and the corresponding centroid is minimized. In each classification run, k-means clustering was restarted 5 times with random initial centroids to avoid convergence to a local minimum. The mean values for the pharmacokinetic model parameters K^{trans} and v_p for each cluster have been calculated.

2.5 Statistical analysis

Results are expressed as mean values ±SD. The group average in each measure was calculated for each time point, and the significance of the changes in these measures, before and after treatment, and between untreated and treaded groups was evaluated by a post-hoc analysis using a one-way non-parametric ANOVA test followed by Dunn's correction for multiple comparisons using a cut-off P-value level of <0.05.

Sample size estimates were performed based on as assumed power of 0.9 and a two-sided significance level of 5%" [43]. All statistical testing was performed using the GraphPad Prism Software (GraphPad Inc., San Diego, CA). Statistical significance was assigned for P values < 0.05.

3. Results

All the twelve mice were successfully imaged twice, before and after the treatment. Quantification of tumor T_1 by MRI at baseline gave a mean ± SD of 940 ±200 msec (both groups, n = 12). Tumor volumes, as determined by manual identification of tumor boundaries from T_{2w} MRI images were similar at baseline, but grew faster in untreated mice in comparison to treated one (Fig. 1A). Tumor growth was significantly reduced after nine days in angiomotin-treated animals, with an average increase of tumor volume of 141 ±52% in comparison to untreated mice (234±70%, P<0.05), as shown in Fig. 1B.

Fig. 2 highlights the intrinsic high heterogeneity in tumor K^{trans} distribution and the proposed clustering approach by applying a k-means alogorithm with three clusters. Figure 2(c,d) show the corresponding blood-pool contrast agent uptake curves for the arterial input function and for three different voxels inside the tumor region, along with the two-compartments model fits. Most notable is that for each single voxel, selected from the three clusterd subsets, is associated a different contrast uptake pattern. Voxels in the peripheral regions exhibited a washout (triangles) or steadily increase (squares) concentration-time pattern (depicted in white and yellow in the cluster map in Fig. 2b), whereas the central voxels (red in the cluster map) were associated with a delayed and very slow uptake of contrast (circles). Fitting of the corresponding ΔR_1 curves to the two-compartment pharmacokinetic Tofts' model resulted in high quality RMSE values (RMSE >0.85 for all the three voxels in Fig. 2d).

Figure 3 shows representative parameter maps of baseline and nine-days post-treatment distribution of tumor K^{trans} and v_p values in a pair of mice (one treated, one untreated), clearly demonstrating an inherent heterogeneity. Prior to treatment, both untreated and treated tumors show voxels with a wide range of K^{trans} values. After nine days, an increase of the number of voxels with high K^{trans} values was seen in the pAmot-treated tumor, but not in the untreated mouse. Representative tumor v_p maps also exhibit spatial heterogeneity (Fig. 3). Treated mouse shows an increase in high v_p values 9 days post-treatment, in comparison to v_p values prior to treatment. Conversely, a slight reduction of the number of voxels with high v_p values was observed for the untreated mouse. Mean values for the parameters obtained from applying the quantitative kinetic modeling, for several descriptive measures of the tumor voxel distributions at baseline (before treatment), and after the DNA-based treatment are reported in Table 1 (K^{trans}) and Table 2 (v_p), respectively. For tumor K^{trans} and v_p estimates, spatial heterogeneity statistics are typically more discriminative than conventional summary statistics.

3.1 Simple summary analysis

No significant differences were found between the two quantitative parameters, with respect to baseline, when mean values were averaged over the whole tumor ROIs (Fig. 4A and 6A). Overall the quantitative estimates from the single whole ROI for treated and untreated group, before and after the treatment, showed similar K^{trans} and v_p tumor average values (Tables 1 and 2).

3.2 Regional rim/core analysis

K^{trans} in tumors, calculated using the rim/core analysis, showed no significant differences between the mean values of treated and untreated mice, for both the rim and the core sub-regions (Table 1 and Fig. 4B). For treated mice, sub-regions v_p estimates were not able to show any difference with respect to baseline (Table 2 and Fig. 6B). A slight reduction was observed in v_p values in the core of the tumor for untreated mice, although not statistically significant.

3.3 Histogram analysis

Figure 4C and Table 1 compare the descriptive measures (skewness and kurtosis) of the K^{trans} histograms before and after the treatment. While the mean skewness of the K^{trans} distribution showed only a slight increase after pAmot treatment, with no significant change for the untreated group, a marked increase in the kurtosis K^{trans} histogram distribution was observed for the treated group, although without a significant change between pre- and post-treatment (mean kurtosis = 84 ±36 and 280 ±215 for the baseline and post treatment values, respectively p>0.05). The same results

were obtained for the v_p histograms indicators, where the most sensitive variable for identifying the difference between the control and the treated group was the kurtosis descriptor (Table 2 and Fig. 6C). A marked and statistically significant increase was observed in the treated group, with the kurtosis of the v_p histogram metric increasing from 11 ±5 to 19 ±11 (p<0.05).

3.4 Clustering analysis

The results of k-means clustering of K^{trans} and v_p provided maps are shown in Tables 1 and 2, respectively. The final number of clusters was varied between two and four to take into account the dependence of the obtained results on the number of clusters.

When tumor voxels were clustered into two distinct clusters, a general trend of increased tumor K^{trans} and v_p estimates was observed within treated group (Fig. 5A and 7A) but without statistically significance. In untreated mice, no significant differences were found with respect to baseline, in any of the two clusters in which K^{trans} and v_p tumor heterogeneity was assessed.

When the number of clusters was increased to three, two out of three tumor sub-regions showed a significant increase of the tumor v_p estimates in treated mice, corresponding to cluster #2 and cluster #3 (Table 2 and Fig. 7B). Pre-treatment tumor K^{trans} were similar for both treated and untreated groups for all the clusters, but a marked increase was observed between pre- and post-treatment tumor K^{trans} values for treated group in both the cluster #2 and cluster #3 (8.1 E-4 ±7.6E-4 and 2.2 E-3 ±3.0E-3 for pre and post treatment, for cluster #2, p>0.05 and 2.3 E-3 ±1.2E-3 and 9.7E-3 ±1.1E-2 for pre and post treatment, for cluster #3, p> 0.05, respectively). A similar trend was observed for tumor v_p values when comparing average pre- and post-treatment for treated group in cluster #2 and #3 (Table 2 and Fig. 7B). In the treated group, the average post-treatment tumor v_p value was 0.09 ±0.07 compared to a baseline v_p of 0.03 ±0.01 (p<0.05) for cluster #2; in addition, the average post-treatment tumor v_p value was 0.21 ±0.17 compared to a baseline v_p of 0.07 ±0.02 (p<0.05) for cluster #3 (Table 2). Tumor v_p values for post-treatment group were significant higher for treated mice in comparison to untreated ones (p<0.05 for both cluster #2 and #3, Table 2 and Fig. 7B).

Clustering tumor voxels into four different sets was not more discriminative of treatment than the three-groups based clustering (Fig. 5C and 7C). In the treated group, tumor K^{trans} values prior to treatment showed a marked increase after 9 days (p>0.05) for cluster #2. Post-treatment tumor v_p measures showed significant changes for treated group, increasing from 0.07 ±0.04 to 0.26 ±0.17 (p>0.05) for cluster #4 (Table 2).

The changes of tumor K^{trans} and v_p, in all the four clusters, did not differ significantly for untreated group mice.

4. Discussion

DCE-MRI has been used in the last decades in a number of pre-clinical and clinical trials to assess the effect of antiangiogenic agents, owing to its ability to provide biomarkers characterizing the tumor vasculature, gaining a strong interest by clinical oncologists. Despite the capability of this non-invasive technique to provide functional parameters which allow to detect early effect and to predict clinical outcome after both cytotoxic, radiation and angiogenesis inhibitor therapies [44], its clinical adoption is still moving slowly, being hampered by the complexity of the data analysis and the reliability of the obtained values. A major issue is related to the heterogeneous nature of the tumor, possessing regions with different permeability/perfusion properties according to the balance between pro- and anti-angiogenic factors which may evolve differently inside the whole tumor and during its growth. This is clearly visible when comparing K^{trans} and v_p tumor maps in which heterogeneous spatially distributed values are seen, both before and after the antiangiogenic treatment (Fig. 3). Such heterogeneity poses big challenges to the definition and selection of the more representative tumor regions. Therefore in the present study various estimated parameters, obtained applying a pharmacokinetic model to the DCE-MRI data, were compared for their effectiveness in identifying significant differences between pAmot-treated and untreated groups. We used a tumor xenograft model to evaluate treatment effects associated with a DNA-based antiangiogenic treatment targeting Amot, an angiostatin receptor overexpressed by endothelial cells of tumor vessels. It was recently shown that anti Amot DNA vaccination significantly delayed the progression of transplantable TUBO tumor in wild-type BALB/c mice with an increase of tumor vessel permeability and vessel diameter [45].

Our findings confirm that in evaluating the effect of an antiangiogenic treatment, the heterogeneity plays an important role that has to be addressed in order to quantify properly the therapeutic response [46]. In the present study mean K^{trans} and v_p values calculated from single three-dimensional ROIs covering the entire tumor were compared with mean values extracted by a rim/core sub-regions analysis, with descriptive measures of histogram characteristics and with mean values obtained subdividing the whole tumor into several sub-regions exploiting a clustering approach. The mean values extracted from a single averaged ROI encompassing the whole tumor did not assess differences in relative changes between treated and untreated mice, due to the level-off of the effects when considering the tumor as a whole. The rim/core sub-regions analysis provided information approximately equal to that obtained from a whole-tumor ROI analysis. These observations agree with previous observation on the mean of K^{trans} distribution [46]. Histogram analysis, as presented in this work, provided one descriptive measure (kurtosis) sensitive for

assessing the efficacy of the antiangiogenic therapy. Previous studies already suggested that histogram analysis applied to quantify the heterogeneity of tumor response to therapy may improve the ability of DCE-MRI to provide useful information on the efficacy of the treatment [47]. Accordingly with previously published results, we observed a large increase in the kurtosis of histograms for the treated mice group [48]. Moreover, the results obtained in this study revealed that also the clustering approach can be a valuable tool to assess the heterogeneity of the tumor allowing the detection of local permeability changes induced by the treatment. K-means clustering is an iterative unsupervised learning process that attempts to determine the best separation of observations, based on the minimizing function (in this study the Euclidean distance) from each input parameter to the cluster centroid. Within the k-means clustering approach, used to partition the pixels in the K^{trans} and v_p maps, pixels were allocated to several sets sharing similar perfusion values. The number of clusters was varied between two and four, and its influence was assessed on the discrimination of DCE-MRI estimates before and after treatment. Only the partitioning of quantitative tumor v_p estimates was able to detect substantial changes before and after treatment for treated mice, and set#2 and #3 within the three-cluster approach detected significant differences between treated and untreated groups.

The clustering approach with only two clusters is likely similar to the rim/core sub-regions analysis, but the number of pixels belonging to one of the two sub-regions is not *a priori* determined, consequently, the ability to detect estimates changes is presumably superior (Fig. 4B and Fig. 5A) . Notably, not all the sets in the three- and four-clusters subdivision changed to the same extent following the treatment, likely due to a not-homogenous immune response in different areas of a tumor. Actually the clustering analysis with three- to four-clusters showed that marked differences were present in clusters with higher K^{trans} and v_p values. In addition, the clustering approach identifies the spatial information of this response. In this study, we observed in the untreated group a marked reduction of voxels with medium-to-high v_p and K^{trans} values (set #2 and #3 for a three-groups subdivision) in the inner regions of the tumor, whereas the more vascularized regions were preserved in the rim region during the tumor growth (Figure 3). Conversely, we observed for treated mice an increase of voxels showing medium K^{trans} and v_p values in the central region of tumor (set #2 for a three-group subdivision, Figure 3). The increased values of tumor K^{trans} and v_p in specific tumor sub-regions correctly reflected previous findings of histological and immunofluorescence analysis, where vascular morphology and vessel permeability were shown to be markedly changed in pAmot-treated tumors [45]. The effect of an enhanced microvasculature permeability following the antiangiogenic treatment has already been reported in several cases, a process known as vasculature normalization [49]. In fact, our findings are in agreement with recently published data

reporting an increase of permeability transfer constant under antiangiogenic treatment by exploiting intermediate MW contrast agents [50, 51].

Therefore, the clustering sub-regions analysis allows detecting subtle drug effects which may be otherwise obscured when analyzing whole tumor ROIs or when employing other conventional summary analysis. In addition, a manual delineation of sub-regions inside the tumor ROIs, like rim and core regions, or the "hot spot" analysis may introduce an individual bias in the calculated values, whereas automatic classification procedures are less operator-dependent [52]. Other groups have also used clustering approaches, but only for discriminating normal from tumor regions [32, 42].

In the present study a blood-pool CA was used to assess tumor vascular permeability estimates, which are lower, in magnitude, than those measured with a low molecular weight CA, due to its larger size. In fact, clinical contrast agents are low molecular contrast agents that rapidly diffuse from the vascular compartment to the interstitial space, resulting in overestimated tumor vascular parameters. They extravasate nonselectively through normal and lesion vasculature, which limits their ability to distinguish between normal and tumor tissues in DCE-MRI. Conversely, the herein used contrast agent, an intermediate MW one, does not extravasate across the normal vasculature and can selectively penetrate tumor vasculature due to tumor vascular hyperpermeability. As a consequence, blood pool CAs have been showed to be more sensitive to changes in vessel permeability than low molecular CAs [12]. Although a smaller amount of CA is expected to extravasate, the sensitivity is higher thanks to the increased relaxation efficiency (and following contrast ability) of the blood-pool CA in comparison to the smaller clinical ones. In addition, we used a low-field 1 Tesla MRI scanner to exploit at best the relaxivity enhancement peak that this class of CAs shows around 40 MHz, providing higher signal enhancements even with lower doses [53]. These inherent properties associated to the larger size of the HSA-supramolecular adducts allow them to be more successful in the evaluation of antiangiogenic treatments [54, 55] as well as for assessing differences in tumor vascularization [56].

This study had some limitations. First, clustering approaches require the definition of the number of sub-regions (clusters) into which the tumor pixels will be grouped. The arbitrary numbers of two, three and four groups were chosen to segment the whole tumor into sub-regions having different permeability/perfusion properties. Ideally the several clusters should reflect tumor sub-regions corresponding to low, medium and high vascularized regions based on the magnitude of K^{trans} and v_p values. A different number of clusters may be more indicated to highlight vascular dissimilarities, although we believe that vascular differences between three to four sub-regions are easier to understand as representative of tumor tissue properties in comparison to higher number of

clusters. Second, the algorithm chosen to perform the clustering step (k-means, Fuzzy C-means, subtractive method) may affect the composition of the tumor sub-regions, partitioning tumor pixels into different subsets, therefore the mean parametric values for each subset may not be equal, but this will be investigated in another study. Analogously, automatic clustering methods (operator independent), able to subdivide automatically the tumor pixels in a different number of sub-regions, were not investigated in this study. Further work is required to establish whether this clustering approach can be extended to other pre-clinical tumor models and for assessing other therapeutic treatments (e.g. chemiotherapy, radiotherapy, or other antiangiogenic protocols). Third, contrast agent was delivered by a manually injection that could introduce variability in the rate and total contrast agent dose administered, despite similar volumes and injection times were employed for all the investigated mice.

5. Conclusion

In conclusion, these results support the view that the heterogeneous nature of the tumor has to be taken in great consideration to properly assess vascular changes induced by antiangiogenic treatments. A clustering analysis was performed on a voxel-by-voxel basis to evaluate spatial distribution of tumor K^{trans} and v_p parametric maps. This study indicates that improvement in the visualization and quantification of heterogeneity in the angiogenic response of tumor to therapy can be assessed by a clustering approach, even when not-homogeneous permeability changes occurred in different areas of a tumor.

References

[1] McDonald DM, Choyke PL. Imaging of angiogenesis: from microscope to clinic. Nat Med 2003;9:713-25.
[2] Abdelrahim M, Konduri S, Basha R, Philip PA, Baker CH. Angiogenesis: an update and potential drug approaches (review). Int J Oncol 2010;36:5-18.
[3] Baluk P, Hashizume H, McDonald DM. Cellular abnormalities of blood vessels as targets in cancer. Curr Opin Genet Dev 2005;15:102-11.

[4] Hylton N. Dynamic contrast-enhanced magnetic resonance imaging as an imaging biomarker. J Clin Oncol 2006;24:3293-8.

[5] Miyazaki K, Collins DJ, Walker-Samuel S, Taylor JN, Padhani AR, Leach MO, et al. Quantitative mapping of hepatic perfusion index using MR imaging: a potential reproducible tool for assessing tumour response to treatment with the antiangiogenic compound BIBF 1120, a potent triple angiokinase inhibitor. Eur Radiol 2008;18:1414-21.

[6] Jonker DJ, Rosen LS, Sawyer MB, de Braud F, Wilding G, Sweeney CJ, et al. A phase I study to determine the safety, pharmacokinetics and pharmacodynamics of a dual VEGFR and FGFR inhibitor, brivanib, in patients with advanced or metastatic solid tumors. Ann Oncol 2011;22:1413-9.

[7] O'Connor JP, Jackson A, Parker GJ, Roberts C, Jayson GC. Dynamic contrast-enhanced MRI in clinical trials of antivascular therapies. Nat Rev Clin Oncol 2012;9:167-77.

[8] Lavini C, de Jonge MC, van de Sande MG, Tak PP, Nederveen AJ, Maas M. Pixel-by-pixel analysis of DCE MRI curve patterns and an illustration of its application to the imaging of the musculoskeletal system. Magn Reson Imaging 2007;25:604-12.

[9] Tofts PS. Modeling tracer kinetics in dynamic Gd-DTPA MR imaging. J Magn Reson Imaging 1997;7:91-101.

[10] Brix G, Semmler W, Port R, Schad LR, Layer G, Lorenz WJ. Pharmacokinetic parameters in CNS Gd-DTPA enhanced MR imaging. J Comput Assist Tomogr 1991;15:621-8.

[11] Yankeelov TE, Luci JJ, Lepage M, Li R, Debusk L, Lin PC, et al. Quantitative pharmacokinetic analysis of DCE-MRI data without an arterial input function: a reference region model. Magn Reson Imaging 2005;23:519-29.

[12] Turetschek K, Preda A, Novikov V, Brasch RC, Weinmann HJ, Wunderbaldinger P, et al. Tumor microvascular changes in antiangiogenic treatment: assessment by magnetic resonance contrast media of different molecular weights. J Magn Reson Imaging 2004;20:138-44.

[13] Farace P, Merigo F, Fiorini S, Nicolato E, Tambalo S, Daducci A, et al. DCE-MRI using small-molecular and albumin-binding contrast agents in experimental carcinomas with different stromal content. Eur J Radiol 2011;78:52-9.

[14] Preda A, Novikov V, Moglich M, Floyd E, Turetschek K, Shames DM, et al. Magnetic resonance characterization of tumor microvessels in experimental breast tumors using a slow clearance blood pool contrast agent (carboxymethyldextran-A2-Gd-DOTA) with histopathological correlation. Eur Radiol 2005;15:2268-75.

[15] Longmire MR, Ogawa M, Choyke PL, Kobayashi H. Dendrimers as high relaxivity MR contrast agents. Wiley Interdiscip Rev Nanomed Nanobiotechnol 2014;6:155-62.

[16] Cheng HL, Wallis C, Shou Z, Farhat WA. Quantifying angiogenesis in VEGF-enhanced tissue-engineered bladder constructs by dynamic contrast-enhanced MRI using contrast agents of different molecular weights. J Magn Reson Imaging 2007;25:137-45.

[17] de Lussanet QG, Langereis S, Beets-Tan RG, van Genderen MH, Griffioen AW, van Engelshoven JM, et al. Dynamic contrast-enhanced MR imaging kinetic parameters and molecular weight of dendritic contrast agents in tumor angiogenesis in mice. Radiology 2005;235:65-72.

[18] Aime S, Gianolio E, Longo D, Pagliarin R, Lovazzano C, Sisti M. New insights for pursuing high relaxivity MRI agents from modelling the binding interaction of Gd(III) chelates to HSA. Chembiochem 2005;6:818-20.

[19] Avedano S, Tei L, Lombardi A, Giovenzana GB, Aime S, Longo D, et al. Maximizing the relaxivity of HSA-bound gadolinium complexes by simultaneous optimization of rotation and water exchange. Chem Commun (Camb) 2007:4726-8.

[20] Woods M, Botta M, Avedano S, Wang J, Sherry AD. Towards the rational design of MRI contrast agents: a practical approach to the synthesis of gadolinium complexes that exhibit optimal water exchange. Dalton Trans 2005:3829-37.

[21] Laurent S, Vander Elst L, Henrotte V, Muller RN. Noncovalent binding of some new lipophilic gadolinium DTPA complexes to human serum albumin. A structure-affinity relationship. Chem Biodivers 2010;7:2846-55.

[22] Geninatti-Crich S, Szabo I, Alberti D, Longo D, Aime S. MRI of cells and mice at 1 and 7 Tesla with Gd-targeting agents: when the low field is better! Contrast Media Mol Imaging 2011;6:421-5.

[23] Padhani AR. MRI for assessing antivascular cancer treatments. Br J Radiol 2003;76 Spec No 1:S60-80.

[24] Armitage PA, Farrall AJ, Carpenter TK, Doubal FN, Wardlaw JM. Use of dynamic contrast-enhanced MRI to measure subtle blood-brain barrier abnormalities. Magn Reson Imaging 2011;29:305-14.

[25] Gillies RJ, Schornack PA, Secomb TW, Raghunand N. Causes and effects of heterogeneous perfusion in tumors. Neoplasia 1999;1:197-207.

[26] Casanovas O, Hicklin DJ, Bergers G, Hanahan D. Drug resistance by evasion of antiangiogenic targeting of VEGF signaling in late-stage pancreatic islet tumors. Cancer Cell 2005;8:299-309.

[27] O'Connor JP, Rose CJ, Waterton JC, Carano RA, Parker GJ, Jackson A. Imaging Intratumor Heterogeneity: Role in Therapy Response, Resistance, and Clinical Outcome. Clin Cancer Res 2015;21:249-57.

[28] Checkley D, Tessier JJ, Kendrew J, Waterton JC, Wedge SR. Use of dynamic contrast-enhanced MRI to evaluate acute treatment with ZD6474, a VEGF signalling inhibitor, in PC-3 prostate tumours. Br J Cancer 2003;89:1889-95.

[29] Galbraith SM, Maxwell RJ, Lodge MA, Tozer GM, Wilson J, Taylor NJ, et al. Combretastatin A4 phosphate has tumor antivascular activity in rat and man as demonstrated by dynamic magnetic resonance imaging. J Clin Oncol 2003;21:2831-42.

[30] Yankeelov TE, Lepage M, Chakravarthy A, Broome EE, Niermann KJ, Kelley MC, et al. Integration of quantitative DCE-MRI and ADC mapping to monitor treatment response in human breast cancer: initial results. Magn Reson Imaging 2007;25:1-13.

[31] Rose CJ, Mills SJ, O'Connor JP, Buonaccorsi GA, Roberts C, Watson Y, et al. Quantifying spatial heterogeneity in dynamic contrast-enhanced MRI parameter maps. Magn Reson Med 2009;62:488-99.

[32] Chang YC, Huang YH, Huang CS, Chang PK, Chen JH, Chang RF. Classification of breast mass lesions using model-based analysis of the characteristic kinetic curve derived from fuzzy c-means clustering. Magn Reson Imaging 2012;30:312-22.

[33] Lavini C, Verhoeff JJ, Majoie CB, Stalpers LJ, Richel DJ, Maas M. Model-based, semiquantitative and time intensity curve shape analysis of dynamic contrast-enhanced MRI: a comparison in patients undergoing antiangiogenic treatment for recurrent glioma. J Magn Reson Imaging 2011;34:1303-12.

[34] Berry LR, Barck KH, Go MA, Ross J, Wu X, Williams SP, et al. Quantification of viable tumor microvascular characteristics by multispectral analysis. Magn Reson Med 2008;60:64-72.

[35] Cavagna FM, Lorusso V, Anelli PL, Maggioni F, de Haen C. Preclinical profile and clinical potential of gadocoletic acid trisodium salt (B22956/1), a new intravascular contrast medium for MRI. Acad Radiol 2002;9 Suppl 2:S491-4.

[36] Rovero S, Amici A, Di Carlo E, Bei R, Nanni P, Quaglino E, et al. DNA vaccination against rat her-2/Neu p185 more effectively inhibits carcinogenesis than transplantable carcinomas in transgenic BALB/c mice. J Immunol 2000;165:5133-42.

[37] Holmgren L, Ambrosino E, Birot O, Tullus C, Veitonmaki N, Levchenko T, et al. A DNA vaccine targeting angiomotin inhibits angiogenesis and suppresses tumor growth. Proc Natl Acad Sci U S A 2006;103:9208-13.

[38] Ramachandran S, Calcagno C, Mani V, Robson PM, Fayad ZA. Registration of dynamic contrast-enhanced MRI of the common carotid artery using a fixed-frame template-based squared-difference method. J Magn Reson Imaging 2014;39:1017.

[39] Brookes JA, Redpath TW, Gilbert FJ, Murray AD, Staff RT. Accuracy of T1 measurement in dynamic contrast-enhanced breast MRI using two- and three-dimensional variable flip angle fast low-angle shot. J Magn Reson Imaging 1999;9:163-71.

[40] Liimatainen T, Sierra A, Hanson T, Sorce DJ, Yla-Herttuala S, Garwood M, et al. Glioma cell density in a rat gene therapy model gauged by water relaxation rate along a fictitious magnetic field. Magn Reson Med 2012;67:269-77.

[41] Ertas G, Gulcur HO, Tunaci M. Improved lesion detection in MR mammography: three-dimensional segmentation, moving voxel sampling, and normalized maximum intensity-time ratio entropy. Acad Radiol 2007;14:151-61.

[42] Michoux N, Simoni P, Tombal B, Peeters F, Machiels JP, Lecouvet F. Evaluation of DCE-MRI postprocessing techniques to assess metastatic bone marrow in patients with prostate cancer. Clin Imaging 2012;36:308-15.

[43] Faul F, Erdfelder E, Lang AG, Buchner A. G*Power 3: a flexible statistical power analysis program for the social, behavioral, and biomedical sciences. Behav Res Methods 2007;39:175-91.

[44] Knopp MV, von Tengg-Kobligk H, Choyke PL. Functional magnetic resonance imaging in oncology for diagnosis and therapy monitoring. Mol Cancer Ther 2003;2:419-26.

[45] Arigoni M, Barutello G, Lanzardo S, Longo D, Aime S, Curcio C, et al. A vaccine targeting angiomotin induces an antibody response which alters tumor vessel permeability and hampers the growth of established tumors. Angiogenesis 2012;15:305-16.

[46] Preda A, Turetschek K, Daldrup H, Floyd E, Novikov V, Shames DM, et al. The choice of region of interest measures in contrast-enhanced magnetic resonance image characterization of experimental breast tumors. Invest Radiol 2005;40:349-54.

[47] Peng SL, Chen CF, Liu HL, Lui CC, Huang YJ, Lee TH, et al. Analysis of parametric histogram from dynamic contrast-enhanced MRI: application in evaluating brain tumor response to radiotherapy. NMR Biomed 2012.

[48] Chang YC, Huang CS, Liu YJ, Chen JH, Lu YS, Tseng WY. Angiogenic response of locally advanced breast cancer to neoadjuvant chemotherapy evaluated with parametric histogram from dynamic contrast-enhanced MRI. Phys Med Biol 2004;49:3593-602.

[49] Jain RK. Normalization of tumor vasculature: an emerging concept in antiangiogenic therapy. Science 2005;307:58-62.

[50] Preda A, Novikov V, Moglich M, Turetschek K, Shames DM, Brasch RC, et al. MRI monitoring of Avastin antiangiogenesis therapy using B22956/1, a new blood pool contrast agent, in an experimental model of human cancer. J Magn Reson Imaging 2004;20:865-73.

[51] Ali MM, Janic B, Babajani-Feremi A, Varma NR, Iskander AS, Anagli J, et al. Changes in vascular permeability and expression of different angiogenic factors following anti-angiogenic treatment in rat glioma. PLoS One 2010;5:e8727.

[52] Fotinos-Hoyer AK, Guermazi A, Jara H, Eckstein F, Ozonoff A, Khard H, et al. Assessment of synovitis in the osteoarthritic knee: Comparison between manual segmentation, semiautomated segmentation, and semiquantitative assessment using contrast-enhanced fat-suppressed T1-weighted MRI. Magn Reson Med 2010;64:604-9.

[53] Botta M, Avedano S, Giovenzana GB, Lombardi A, Longo D, Cassino C, et al. Relaxometric Study of a Series of Monoaqua Gd-III Complexes of Rigidified EGTA-Like Chelators and Their Noncovalent Interaction with Human Serum Albumin. European Journal of Inorganic Chemistry 2011:802-10.

[54] Raatschen HJ, Fu Y, Brasch RC, Pietsch H, Shames DM, Yeh BM. In vivo monitoring of angiogenesis inhibitory treatment effects by dynamic contrast-enhanced computed tomography in a xenograft tumor model. Invest Radiol 2009;44:265-70.

[55] Wilmes LJ, Pallavicini MG, Fleming LM, Gibbs J, Wang D, Li KL, et al. AG-013736, a novel inhibitor of VEGF receptor tyrosine kinases, inhibits breast cancer growth and decreases vascular permeability as detected by dynamic contrast-enhanced magnetic resonance imaging. Magn Reson Imaging 2007;25:319-27.

[56] Bandini S, Curcio C, Macagno M, Quaglino E, Arigoni M, Lanzardo S, et al. Early onset and enhanced growth of autochthonous mammary carcinomas in C3-deficient Her2/neu transgenic mice. Oncoimmunology 2013;2:e26137.

Table 1
Group-averaged descriptive measures of tumor K^{trans}

K^{trans} (min^{-1})		Treated		Untreated	
		PRE	POST	PRE	POST
Conventional analysis					
Mean		2.0 ±1.7E-04	1.4 ±1.0E-04	2.6 ±1.9E-04	2.7±1.6E-04
Sub-regions analysis					
Rim		2.4 ±2.1E-04	2.1 ±1.3E-04	2.9 ±2.2E-04	3.0±1.7E-04
Core		1.5 ±1.3E-04	2.0 ±2.5E-04	2.2 ±1.7E-04	1.7 ±1.2E-04
Histogram analysis					
Skewness		7 ± 2	13 ± 6	9 ± 5	12 ± 6
Kurtosis		84 ± 36	280 ± 215	125 ± 109	138 ± 73
Clustering analysis					
Cluster	#1	1.6 ±1.4E-04	1.5 ± 1.1E-04	1.7 ± 1.1E-04	2.0 ±1.3E-04
	#2	24±36E-04	59 ± 67E-04	41 ± 62E-04	45± 30E-04
	#1	1.1 ± 0.6E-04	1.3 ± 1.0E-04	1.1 ± 0.6E-04	1.5 ± 0.9E-04
	#2	8.1± 7.7E-04	22 ± 30E-04	6.2 ± 2.7E-04	10 ± 6E-04
	#3	23 ± 12E-04	100 ± 110E-04	45 ± 59E-04	76 ± 25E-04
	#1	0.8 ± 0.6E-04	1.1 ± 0.8E-04	0.9 ± 0.6E-04	1.2 ± 0.8E-04
	#2	4.7 ± 6.0E-04	15 ± 22E-04	5.2 ± 3.3E-04	9.7 ± 4.7E-04
	#3	15 ± 21E-04	37 ± 55E-04	23 ± 30E-04	27 ± 11E-04
	#4	47 ± 59E-04	90 ± 110E-04	81 ± 86E-04	120±110E-04

Values are grouped means with SD from all the animals studied. Number of mice: N=6 for the pAmot-treated group, N=6 for the untreated group.

Table 2
Group-averaged descriptive measures of tumor v_p

v_p		Treated		Untreated	
		PRE	POST	PRE	POST
Conventional analysis					
Mean		0.04 ± 0.02	0.04 ± 0.02	0.03 ± 0.02	0.03 ± 0.01
Sub-regions analysis					
Rim		0.04 ± 0.02	0.04 ± 0.02	0.03 ± 0.02	0.03 ± 0.01
Core		0.03 ± 0.02	0.04 ± 0.04	0.03 ± 0.02	0.02 ± 0.01
Histogram analysis					
Skewness		3 ± 2	3 ± 1	3 ± 1	3 ± 2
Kurtosis		11 ± 5	19 ± 11[a]	14 ± 4	17 ± 6
Clustering analysis					
Cluster	#1	0.02 ± 0.01	0.03 ± 0.04	0.02 ± 0.01	0.01 ± 0.01
	#2	0.07 ± 0.03	0.14 ± 0.10	0.07 ± 0.03	0.05 ± 0.02
	#1	0.01 ± 0.01	0.02 ± 0.02	0.01 ± 0.01	0.01 ± 0.01
	#2	0.03 ± 0.01	0.09 ± 0.07[a]	0.03 ± 0.01	0.03 ± 0.01[b]
	#3	0.07 ± 0.02	0.21 ± 0.17[a]	0.07 ± 0.03	0.06 ±.0.02[b]
	#1	0.01 ± 0.01	0.01 ± 0.05	0.01 ± 0.01	0.01 ± 0.01
	#2	0.03 ± 0.01	0.04 ± 0.03	0.02 ± 0.01	0.02 ± 0.01
	#3	0.05 ± 0.02	0.10 ± 0.07	0.04 ± 0.02	0.04 ± 0.01
	#4	0.07 ± 0.04	0.26 ± 0.17[a]	0.08 ± 0.04	0.08 ± 0.03

Values are grouped means with SD from all the animals studied. Number of mice: N=6 for the pAmot-treated group, N=6 for the untreated group. [a] Statistically significant difference between pre- and post-treatment studies, P<0.05. [b] Statistically significant difference between treated and untreated groups in post-treatment studies.

Figure Legends

Figure 1 Inhibition of tumor growth in mice by angiomotin vaccine treatment. (A) Tumor volumes before and after treatment show a significant increase for untreated mice (P<0.01). (B) Percentage change in tumor volume after angiomotin treatment show significant inhibition for treated mice in comparison with control (Δ = 141 ±52% and 234±70% for treated and untreated, respectively; P<0.05).

Figure 2 Color maps of quantitative tumor K^{trans} (min^{-1}) for a representative untreated mouse (A). Tumor voxels were clustered into three subsets according to their K^{trans} values by a k-means algorithm and color coded in red, green and blue for subsets #1, #2 and #3, respectively (B). Representative tracer uptake curves as changes in relaxation rate (ΔR_1) obtained from (C) the AIF (cross symbol) and (D) single voxels selected from the three subsets with the corresponding fit. The three selected voxels belong to tumor regions that have been clustered as set #1 (squared symbols), set #2 (circle symbols) and set #3 (triangle symbols).

Figure 3 Representative quantitative tumor K^{trans} maps and corresponding cluster using a three-clusters set (top), and quantitative tumor v_p maps with corresponding clustering using a three-clusters set (bottom) of a transaxial section through the tumor of one treated (left) and one untreated (right) mouse before and after the treatment. Parametric maps are overimposed on the T_{2w} anatomical image and shown inside the tumor region. Tumor pixels have been clustered into three sub-regions color-coded in red, green and blue, corresponding to groups with low-, medium- and high-values of K^{trans} and v_p estimates, respectively.

Figure 4 Bar graph plots of quantitative tumor K^{trans} (min^{-1}) estimates calculated by (A) simple summary statistics, (B) sub-regions analysis, (C) histogram analysis from averaged-groups treated and untreated mice shown in Table 1. Values are shown as mean ±SEM.

Figure 5 Bar graph plots of quantitative tumor K^{trans} (min^{-1}) estimates calculated by clustering analysis exploiting the following number of clusters: (A) two-clusters, (B) three-clusters, (C) four-cluster, from averaged-groups treated and untreated mice shown in Table 1. Values are shown as mean ±SEM.

Figure 6 Bar graph plots of quantitative tumor v_p estimates calculated by (A) simple summary statistics, (B) sub-regions analysis, (C) histogram analysis from treated and untreated mice shown in Table 2. Values are shown as mean ±SEM where $*P< 0.05$.

Figure 7 Bar graph plots of quantitative tumor v_p estimates calculated by clustering analysis exploiting the following number of clusters: (A) two-clusters, (B) three-clusters, (C) four-cluster, from averaged-groups treated and untreated mice shown in Table 1 Values are shown as mean ±SEM where $*P< 0.05$.
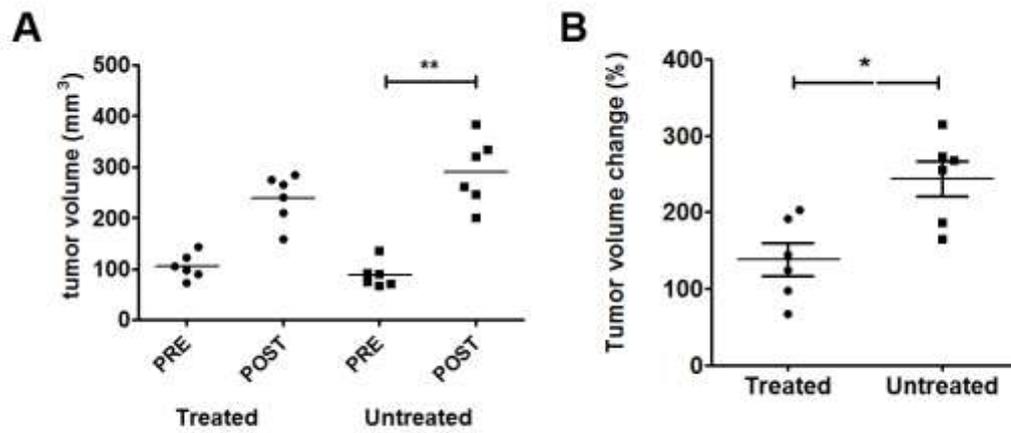
Figure 1 Inhibition of tumor growth in mice by angiomotin vaccine treatment. (A) Tumor volumes before and after treatment show a significant increase for untreated mice in comparison to untreated ones (P<0.01). (B) Percentage change in tumor volume after angiomotin treatment show significant inhibition for treated mice in comparison with control (Δ = 141 ±52% and 234 ±70% for treated and untreated, respectively; P<0.05).
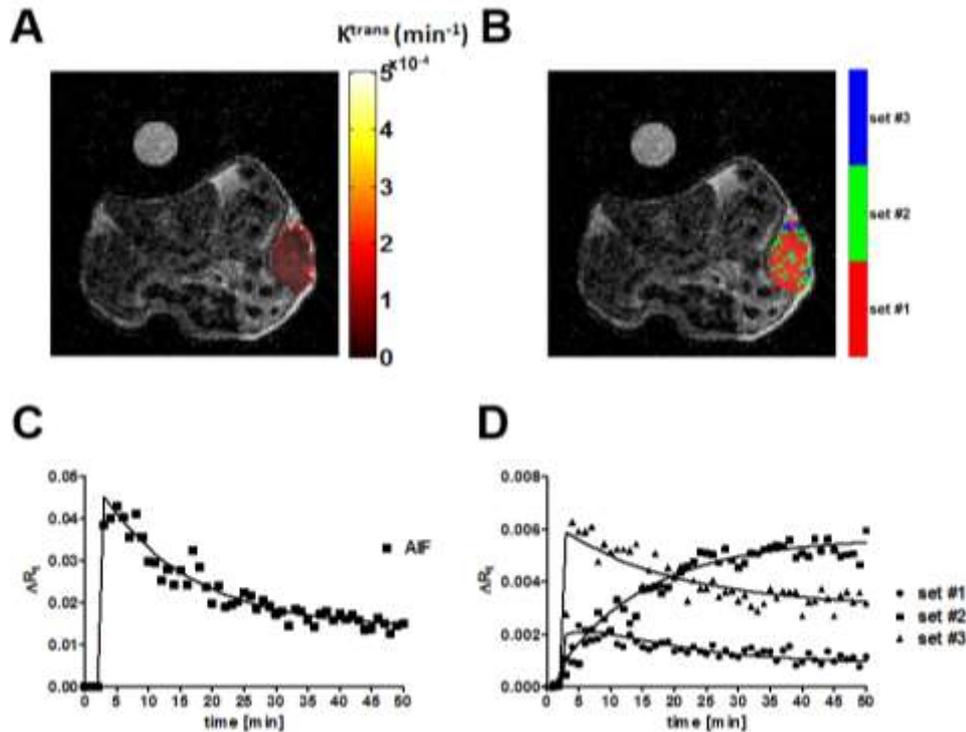
Figure 2 Color maps of quantitative tumor K^{trans} (min^{-1}) for a representative untreated mouse (A).

Tumor voxels were clustered into three subsets according to their K^{trans} values by a k-means

algorithm and color coded in red, yellow and white for subsets #1, #2 and #3, respectively (B).

Representative tracer uptake curves as changes in relaxation rate (ΔR_1) obtained from (C) the AIF

(cross symbol) and (D) single voxels selected from the three subsets with the corresponding fit. The

three selected voxels belong to tumor regions that have been clustered as set #1 (squared symbols),

set #2 (circle symbols) and set #3 (triangle symbols).
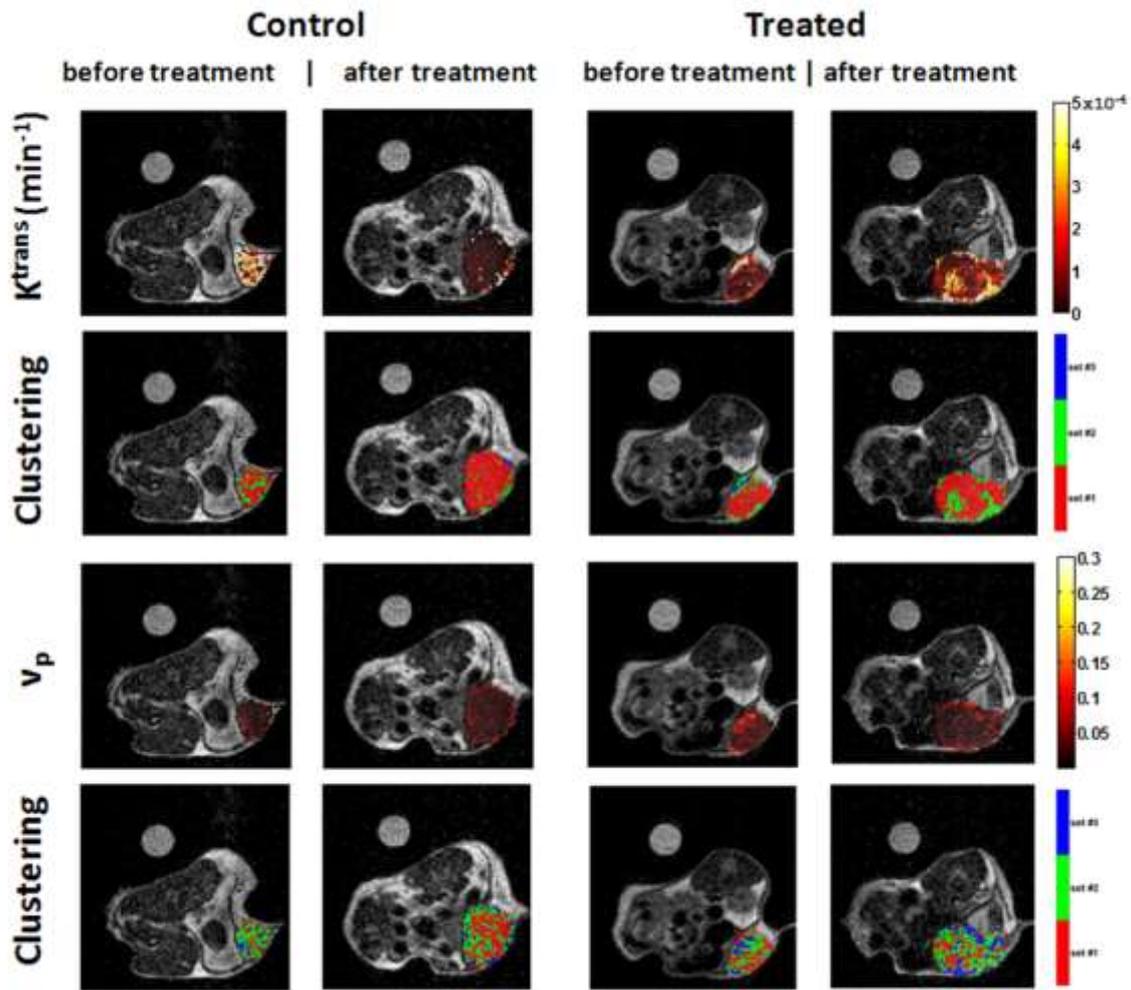
Figure 3 Representative quantitative tumor K^{trans} maps and corresponding cluster using a three-clusters set (top), and quantitative tumor v_p maps with corresponding clustering using a three-clusters set (bottom) of a transaxial section through the tumor of one pAmot-treated (left) and one untreated (right) mouse before and after the treatment. Parametric maps are overimposed on the T_{2w} anatomical image and shown inside the tumor region. Tumor pixels have been clustered into three sub-regions color-coded in red, green and blue, corresponding to groups with low-, medium- and high- values of K^{trans} and v_p estimates, respectively.

Figure 4 Bar graph plots of quantitative tumor K^{trans} estimates calculated by (A) simple summary statistics, (B) sub-regions analysis, (C) histogram analysis from averaged-groups treated and untreated mice shown in Table 1. Values are shown as mean ±SEM.
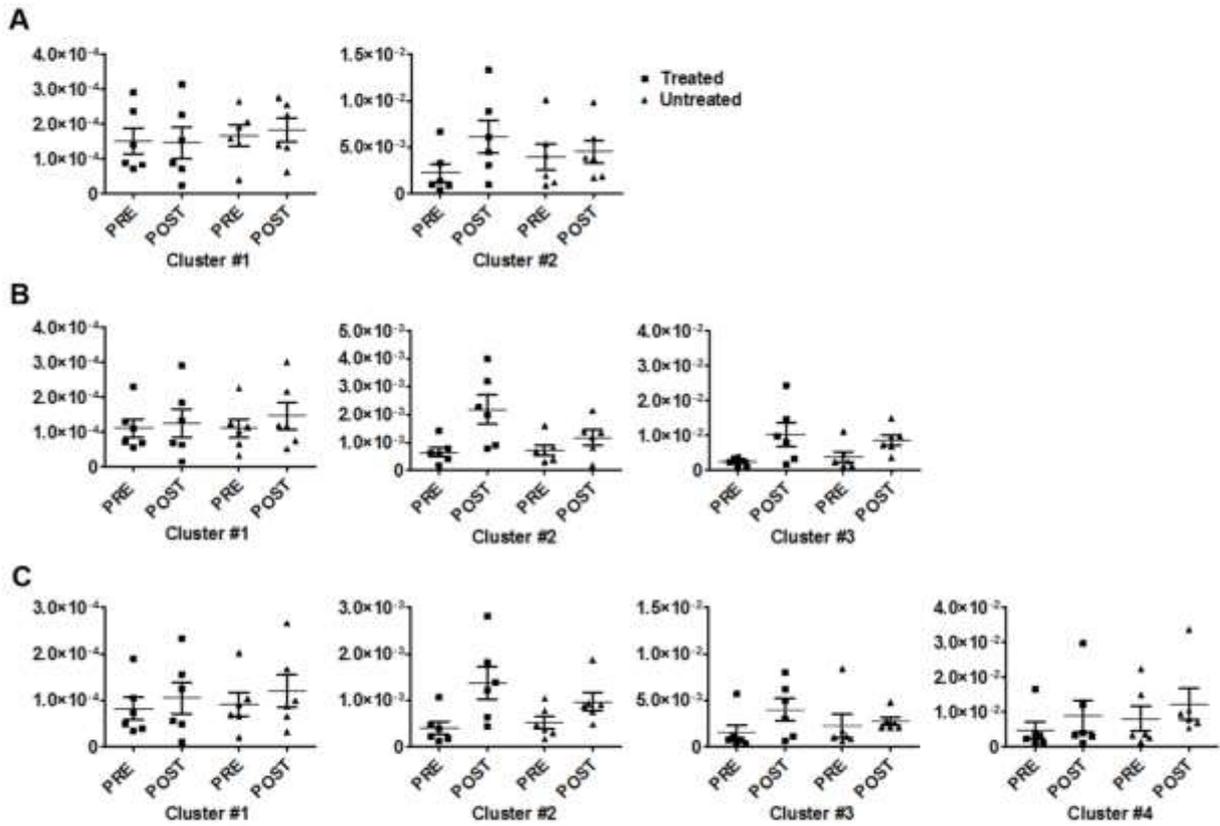
Figure 5 Bar graph plots of quantitative tumor K^{trans} estimates calculated by clustering analysis exploiting the following number of clusters: (A) two-clusters, (B) three-clusters, (C) four-cluster, from averaged-groups treated and untreated mice shown in Table 1. Values are shown as mean ±SEM.
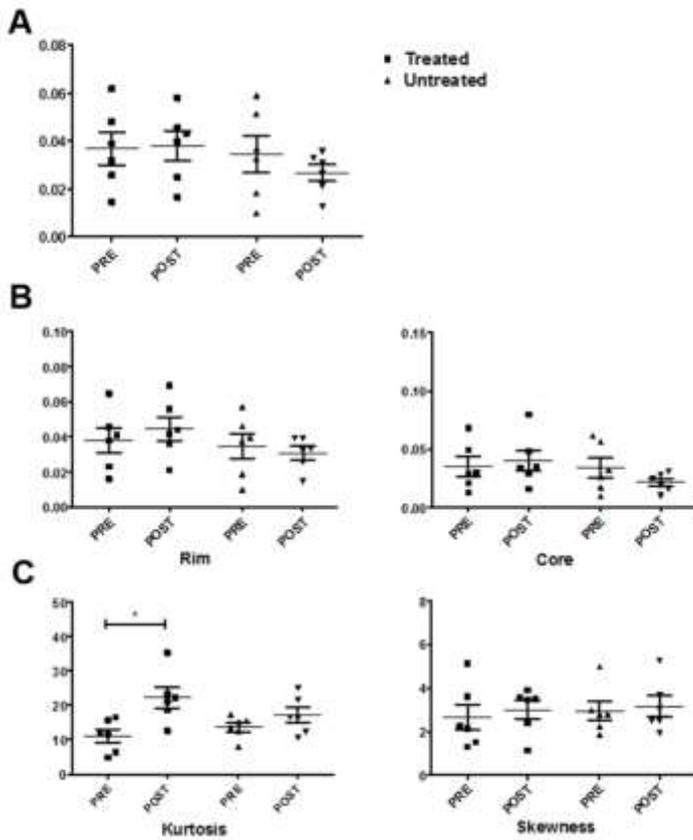
Figure 6 Bar graph plots of quantitative tumor v_p estimates calculated by (A) simple summary statistics, (B) sub-regions analysis, (C) histogram analysis from treated and untreated mice shown in Table 2. Values are shown as mean ±SEM where *P< 0.05.
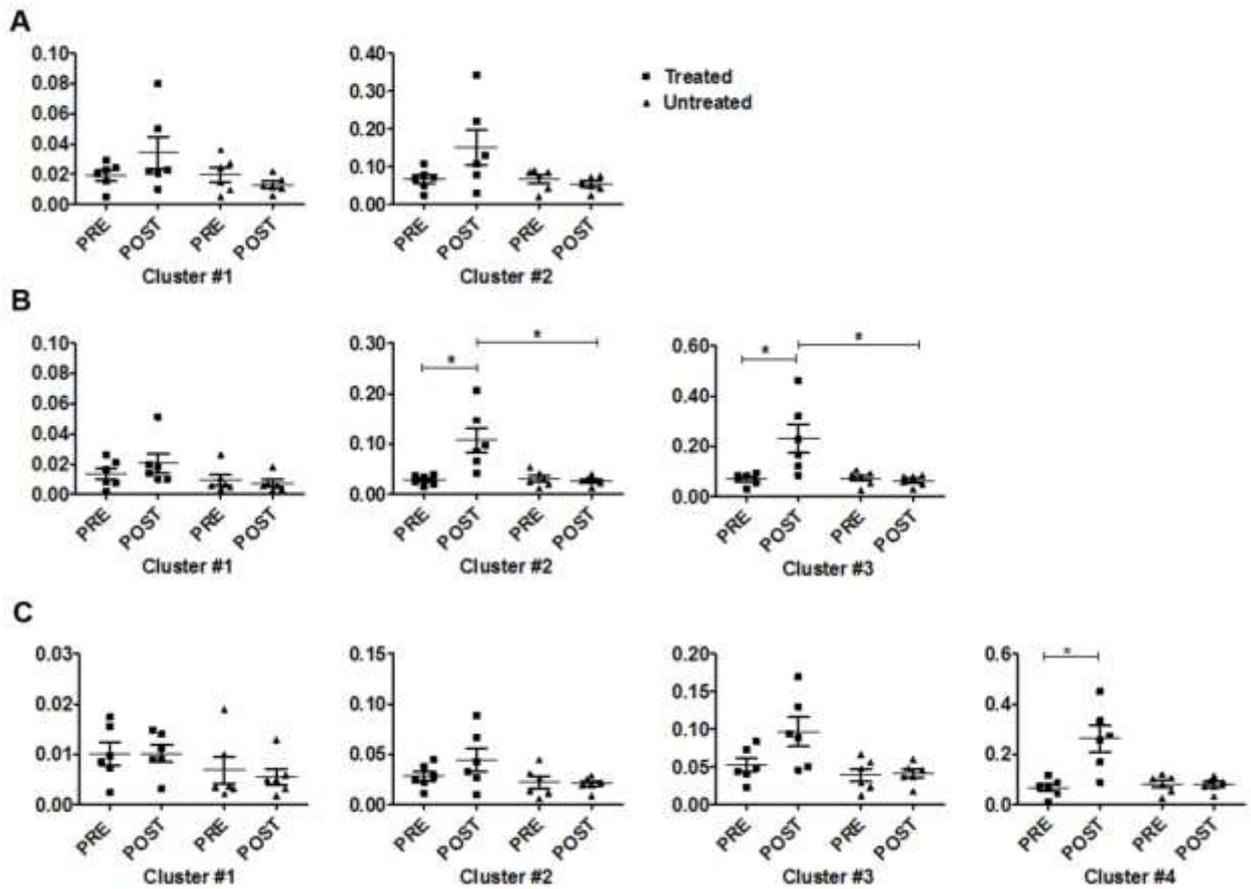
Figure 7 Bar graph plots of quantitative tumor v_p estimates calculated by clustering analysis exploiting the following number of clusters: (A) two-clusters, (B) three-clusters, (C) four-cluster, from averaged-groups treated and untreated mice shown in Table 1. Values are shown as mean ±SEM where *P< 0.05.